



www.sciencemag.org/cgi/content/full/science.1208898/DC1

Supporting Online Material for

Lithospheric Thinning Beneath Rifted Regions of Southern California

Vedran Lekic,* Scott W. French,[†] Karen M. Fischer

*To whom correspondence should be addressed. E-mail: vedran_lekic@brown.edu

Published 6 October 2011 on *Science Express*
DOI: 10.1126/science.1208898

This PDF file includes:

Materials and Methods
SOM Text
Figs. S1 to S10
References

Materials and Methods

We constructed Sp and Ps receiver functions using a semi-automated waveform analysis procedure applied previously to single station stacks across North America (14), with the modification that the deconvolution is carried out for each source receiver pair using a MATLAB implementation (31) of the extended-time multi-taper cross-correlation method (32) with a time-bandwidth product of 2.5, a moving window length of 50 s, and 25% overlap between time windows. This process yields >52,000 individual Sp receiver functions.

To create the common conversion-point (CCP) images, receiver function amplitudes were migrated into a physical volume defined by depth, latitude and longitude (r, θ, ϕ), using 1D ray tracing along the backazimuth and ray parameter of the parent S phase and a velocity model for each station that is based on crustal Vp and Vp/Vs determined from H- κ stacking (33) of Ps waveforms for each station in our study, mantle Vs from high-resolution surface-wave tomography (10) and Vp/Vs ratios from teleseismic body-wave tomography (11). The volume beneath Southern California was discretized every 0.5 km in depth, and 0.1° in latitude and longitude. At each discrete location (r_k, θ_k, ϕ_k), the CCP stack was calculated by a weighted average of all receiver functions at that depth, where the weighting factor $\gamma(\Delta)$ was determined by evaluating a normalized cubic spline at the horizontal distance (Δ) of each migrated RF ray from the physical point (r_k, θ_k, ϕ_k) of the CCP stack.

The knot spacing Δ^0 , which defines the cubic spline, increases with depth and is given by:

$$\Delta^0 = \frac{1}{2} \sqrt{\left(\frac{\lambda}{3} + r_k\right)^2 - r_k^2},$$

where λ is the wavelength of S waves at their dominant period (~ 11 sec). This definition of the knot spacing Δ^0 was chosen so that the weighting factor is related to the zero-offset Fresnel zone half width at that depth. The Fresnel zone half width is defined by:

$$\text{FZHW}(d) = \sqrt{(d + r_k)^2 - r_k^2},$$

where d is typically taken to be $\lambda/4$ or $\lambda/2$. The normalized cubic spline with knot spacing Δ^0 defines the weight of individual receiver functions in the CCP stack at a given point.

This weight, $\gamma(\Delta)$, is given by:

$$\gamma(\Delta) = \begin{cases} \frac{3}{4} \bar{\Delta}^3 - \frac{3}{2} \bar{\Delta}^2 + 1, & \bar{\Delta} \leq 1 \\ \frac{1}{4} (2 - \bar{\Delta})^3, & 1 \leq \bar{\Delta} \leq 2 \\ 0, & \bar{\Delta} > 2 \end{cases}$$

where $\bar{\Delta} = \Delta/\Delta^0$. Our choice of Δ^0 means that $\gamma(\Delta) \approx 0.5$ when $\Delta = \text{FZHW}(\lambda/4)$ and $\gamma(\Delta) \approx 0$ when $\Delta \geq \text{FZHW}(\lambda/2)$. When $\Delta > 2\Delta^0$, $\gamma(\Delta)$ is zero.

For locations at which more than 35 individual receiver functions contributed to the image (i.e. 35 receiver functions with $\gamma(\Delta)$ greater than zero), an LAB depth was determined through an automatic picking algorithm that identified the LAB as the median depth of the 25 most negative values in the vertical CCP profile beneath each surface location in the 30 to 110 km depth range (see Figure S7).

SOM Text

Discussion of Resolution, Uncertainty, and Interpretation

In this section, we assess and, where possible, quantify the reliability of the images and conclusions presented in the main text. We begin by justifying the interpretation of the large negative phase in the common conversion point (CCP) stacks as the lithosphere-asthenosphere boundary (LAB). We then probe the quality of the crustal model developed with H- κ stacking that we use to migrate the deconvolved time-domain waveforms into the physical volume beneath Southern California. We then proceed to quantify the uncertainty in LAB depth from uncertainty in the velocity model used in migration and from data limitations. We investigate the resolving power of our dataset by generating and migrating synthetic Sp receiver functions. Finally, we explore the meaning of the crustal stretching estimates within the Salton Trough derived from our lithospheric thinning constraints by comparing inferred sediment thickness with values predicted by the instantaneous stretching model (6), assuming a range of plausible initial lithospheric thicknesses, and crustal and sediment densities.

Why is the negative phase in Sp receiver functions likely to be the LAB?

We attribute the large negative Sp phases in the 40-100 km depth range to the velocity drop across the lithosphere-asthenosphere boundary. This conclusion is based on a set of synthetic exercises that explored the strength of the velocity drop with depth necessary to produce the observed negative phase on Sp receiver functions. This analysis, described below, shows that the magnitude of the velocity drop is approximately the same as the magnitude of the total velocity drop from the lithosphere to the asthenosphere, as constrained by regional high-resolution surface wave tomography (10). The Sp data are therefore consistent with the lithosphere-asthenosphere velocity contrast seen in the tomography, but imply that this drop in velocity occurs over a much smaller depth range than is resolvable by the tomography.

In Figure S1, we show the observed Sp receiver functions at two stations of the Southern California Seismic Network: VTV, located in the Mojave Block, and DRE, located in the Salton Trough. Here, all deconvolved Sp waveforms for each station were summed together, averaging over lateral variations in discontinuity structure. Bootstrapping was carried out to ascertain the uncertainty in the receiver function at each depth. We constructed 100 sets of receiver functions by randomly re-sampling the entire dataset consisting of all receiver functions (one for each earthquake) at a given station. The means of each constructed dataset represent 100 estimates of the true receiver function, and their mean is plotted in black in Figure S1. Their standard deviation represents the uncertainty on the true receiver function, and is denoted by the dashed lines in Figure S1.

In Figure S1 we also plot synthetic receiver functions expected for a velocity drop of 2, 5 and 8% across an LAB at a depth of 40 km for DRE and 70 km for VTV (with the Moho at 20 km and 30 km, respectively). Crustal properties are: compressional velocity (V_p) = 5.66 km/s; shear velocity (V_s) = 3.2 km/s; density (ρ) = 2.8 g/cc. Lithospheric properties are: V_p = 7.92 km/s; V_s = 4.4 km/s; ρ = 3.3 g/cc. Percent drops across the LAB are with respect to lithospheric velocities; density is not changed across the LAB. For each station and model, we calculated synthetic 3-component seismograms using a propagator matrix method (34) for each earthquake present in the actual dataset, ensuring

that the synthetics correspond to an identical set of ray parameters as the data. The synthetics were then processed in the same way as the data in order to create Sp receiver functions. The receiver functions were migrated to depth using the synthetic velocity model.

The observed Sp phases in the station stacks are best fit by a shear velocity drop of 8%, and their one standard deviation uncertainties require a velocity drop of more than 5% (Figure S1). Furthermore, the 5% lower bound may well be an underestimate because the velocity drop across the LAB is not likely to be instantaneous in depth, and increasing the depth range over which the velocity drop is distributed tends to weaken the amplitude of the Sp conversion (e.g. 35). The amplitudes of the observed positive phases from the crust-mantle boundary (Moho) are somewhat smaller than the Moho phases predicted by the assumed velocity models. However, this discrepancy does not significantly affect the estimation of velocity drops at the LAB (36).

The Sp station stacks are similar to the CCP stacks directly beneath each station (Figure S1), particularly at shallower depths. Because the CCP stack beneath each station is not sampling the same structure as the station stack (the latter includes contributions from structure away from the station) and because this difference increases with depth, the CCP stack and the station stack look less similar at greater depths. Nonetheless, the CCP LAB phase at DRE matches the station stack and is best fit by an 8% velocity drop. The CCP LAB phase at VTV lies within the one standard deviation uncertainties of the VTV station stack, even though it would be best fit by a slightly deeper and weaker (5% drop) discontinuity.

In Vs tomography (10), typical maximum shear wavespeeds in the lithosphere beneath the region are 4.3-4.5 km/s, and typical maximum velocity drops from the lithosphere to the asthenosphere are ~0.3-0.5 km/s. This result means that the velocity contrast required to produce the phases we observe in our Sp receiver functions accounts for most (or all) of the 7-9% drop in Vs across the LAB expected from tomography.

How sharp is the LAB and why would it correspond to a rheological boundary?

If the velocity drop at the LAB is limited to 10% or less, slightly higher than the maximum implied by tomographic models (10), synthetic Sp receiver functions (e.g. 35) indicate that the LAB velocity gradient must occur over ~30 km or less.

What are the physical and chemical factors that could produce such a sharp velocity gradient at the lithosphere-asthenosphere boundary in a rift setting? Unlike in cratonic and other stable continental regions, it is not inconceivable that asthenospheric upwelling associated with continental rifts can result in steep thermal gradients (e.g. 2) that, when converted to shear velocity using experimentally-determined scaling relationships (e.g. 37), may be sufficiently large and localized in depth to produce the Sp conversions that we image beneath the Salton Trough. However, in the unrifted regions of our study area, the absence of upwelling would result in isotherms that are less concentrated in depth and that would be less likely to produce the sharp observed velocity gradients. In unrifted regions, other mechanisms such as asthenospheric partial melt, chemical stratification (a drier lithosphere over a hydrated asthenosphere) and/or sharp vertical transitions in anisotropy are probably required. It is possible that the “LAB” imaged beneath rifted and unrifted regions may reflect different combinations of mechanisms, although small

fractions of partial melt directly below the LAB could explain observed velocity gradients across the entire study region (e.g. 38,39).

In general, it is reasonable to assume that the seismologically observed LAB corresponds to a rheological boundary. If gradients of temperature with depth are large enough to produce the shear velocity drop, the seismic LAB would correspond to a rheological boundary due to the exponential temperature-dependence of viscosity (e.g. 37,40). If, on the other hand, a small amount of melt is necessary to explain the abruptness and magnitude of the velocity drop, the seismic LAB would also indicate a rheological boundary, because even a small amount of melt can result in large decrease of viscosity (e.g. 41,42). Even if the velocity drops are caused by the presence of volatiles such as water, the seismic LAB would again imply a rheological boundary because small amounts of volatiles are effective at reducing viscosity (e.g. 43). Finally, if abrupt changes in seismic anisotropy give rise to the seismic LAB phases we observe, it is still likely that the seismic LAB corresponds to a rheological boundary. If lattice-preferred orientation dominates, then abrupt changes in anisotropy could be due either to changes in the strain field (e.g. 44), or because of changes in the slip system, for example due to hydration (e.g. 45). Both of these cases would imply a rapid change in viscosity across the observed LAB.

Crustal structure

In the velocity model used to migrate the S_p receiver functions to form the three-dimensional CCP stack images, we employ per-station estimates of crustal thickness and V_p/V_s ratios determined from H- κ stacking (33) of P_s waveforms for each of the seismic stations used in our study. Here we assess the reliability of these estimates of crustal structure.

In Figure S2, we show the histograms of crustal thickness and V_p/V_s ratios, which show distributions in line with those expected for the region from other studies, for example the SCEC-CVM-H model (27). Crustal thickness varies from just under 20 km to 40 km, with the thickest crust observed beneath the Peninsular and Transverse Ranges, and the thinnest crust observed beneath the Continental Borderlands and the Salton Trough. Crustal thicknesses of ~30 km are found beneath the Mojave Block and the Los Angeles Basin. Typical crustal V_p/V_s ratios are in the 1.70-1.75 range, with higher values observed beneath the Salton Trough and in the Los Angeles Basin.

In Figure S2, we also compare inferred depths to the Moho to values in the SCEC-CVM-H model (27). We find very good agreement between our Moho depth determinations and those in SCEC-CVM-H, although the range of Moho depths is 5-10% greater in our model than would be inferred from SCEC-CVM-H. This discrepancy is most likely because our measurements represent point constraints, whereas the Moho surface in SCEC-CVM-H is smoothed and interpolated from data spanning Southern California. Least-squares fit of a line to the H- κ and SCEC-CVM-H crustal thicknesses yields a slope of 1.06 and a y-intercept of -0.98. The standard deviation of the residuals from the best-fit line is only 2.75 km. The average difference between the H- κ and SCEC-CVM-H crustal thicknesses is 0.69 km with a standard deviation of 2.76 km. For typical crustal velocities and the range of ray parameters used in our study, a change in crustal thickness of 2.75 km will change S_p -S time by 0.35 to 0.45 s, which would displace the LAB by less than 3 km.

Uncertainty due to the velocity model used in migration

In order to quantify the worst-case scenario for error in LAB depth introduced by migration through an inaccurate model of crustal and mantle velocity structure, we duplicated the procedure used to create the map of LAB depth (Figure 1 of main text), except that the migration was carried out through a uniform 1D model: the SCEC-1D profile in the crust (46), and AK135 structure in the mantle (47). The LAB depths obtained with the 1D model were subtracted from the LAB depths determined by migration through the preferred 3D model, and the resulting differences are displayed in Figure S3. Making the easily justified assumption that the 3D model more accurately represents true crustal and mantle elastic structure beneath Southern California, the differences in depth represent very generous upper limits on errors that migration through an inaccurate velocity model can introduce.

The histogram in Figure S3 (left panel) shows that the LAB depths determined via migration through a 1D model are systematically deeper by 4.4 km than those migrated in the more realistic 3D model. Once this bias is accounted for, the migration model results in less than 5 km difference in LAB depth for more than 80% of bins in which the LAB is determined. This result is shown in the right panel of Figure S3, where we plot the proportion of all bins in which the difference in LAB depth is within a specified distance from this mean. Nevertheless, for <5% of locations, changing the migration model leads to very different LAB depths. These are associated with regions where the identification of an LAB phase is ambiguous and should not be interpreted to represent true uncertainty on LAB depth due to migration error. These anomalous cases are found preferentially in two types of locations: 1) boundaries of regions that are characterized by different LAB depths, in which case the large difference in LAB depth results from shifting the boundaries laterally, rather than from actual mislocation of the LAB phase in depth; 2) the edges of our study region, where the LAB is likely to be constrained by data from few stations and by conversions from parent phases with large ray parameters, which make the path geometries and Sp-S times more sensitive to variations in velocity structure. While the images migrated in the 1D and 3D model look very similar, migration in the 3D model yields discontinuities that are sharper and better defined. This finding enhances our confidence that the 3D model better represents real crust and mantle structure.

This analysis indicates that the relative uncertainty in LAB depth (uncertainty between points in the model versus uncertainty in absolute depth) due to crust and mantle structure is less than 5 km over most of the model. In fact, 5 km is in general an over-estimate of relative uncertainty due to structure, because the crustal model from H- κ stacking assumed in the 3D model matches other constraints on crustal structure (see preceding section) and is clearly superior to SCEC-1D, especially in regions of highly anomalous crustal thickness such as the Salton Trough.

Uncertainty due to Sp receiver function CCP stack limitations

Having estimated outer limits on uncertainty due to crust and mantle velocities, here we quantify the uncertainty in LAB depth determinations that arise from limitations of the Sp receiver function CCP stacks and/or the strength of the conversion across the LAB.

We considered variations in data coverage by plotting the hit count of ray-theoretical piercing points for our Sp dataset in 10 km bins at depths of 40, 60, 80 and 120 km (Figure S4). We found that at these depths, data coverage is excellent throughout the region of study. Because the bin size in Figure S4 is smaller than the Fresnel zone width of the Sp receiver functions, small gaps in data coverage do not prevent us from obtaining a reliable estimate of LAB depth. Furthermore, variations in data coverage do not exhibit any correlation with lithospheric thickness, further supporting the conclusion that data coverage is sufficient for the LAB depth interpretations presented in the main text.

We also estimated the uncertainty in LAB depth introduced by the band-limited nature of the Sp receiver function signals. We measured the half-width of the LAB phase at half its maximum amplitude under each point of our model, and plotted in Figure S5 (top panel). We consider half of the half-width to be a sensible outer bound on how much the LAB interface could be displaced in depth while remaining consistent with the observed LAB phase for a given model bin. Underneath most areas, this uncertainty would be less than ± 10 km; significantly, the phase width beneath the Salton Trough and the Continental Borderland is even narrower, with uncertainty < 5 km. Note that the uncertainty in LAB depth that would be inferred from the one standard deviation bootstrap uncertainties in the station-averaged receiver functions for VTV and DRE (Figure S1) is 7-8 km, reinforcing the idea that ± 10 km is a generous uncertainty estimate.

Because very weak phases might not be robust, we also examined the strength of the LAB phase. We found that 0.04 (relative to the parent S wave) is the minimum amplitude of a phase that can be robustly identified given the typical oscillations present in the CCP stacks; therefore, we did not determine an LAB depth in profiles where the largest negative phase does not cross this threshold. On the other hand, anomalously large negative phases are sometimes found beneath locations that are poorly sampled, and may not represent true strength of the velocity jump across the LAB. The amplitude of the LAB phase across Southern California is plotted in Figure S5 (bottom panel), and varies from ~ 0.05 - 0.12 across most of the region of study. Importantly, the strength of the LAB phase is not correlated with its depth, so systematic variations in the strength of the LAB phase are highly unlikely to bias any of the conclusions presented in the main text.

Resolution

To test the spatial resolution of crust and mantle structure provided by Sp phases, we calculated synthetic seismograms through candidate 2D models using the SPECFEM2D code (48) (available from www.geodynamics.org). This method allows accurate calculation of wave propagation through complex and heterogeneous velocity structures (e.g. 48) such as can be expected from the strong lateral variations in crustal and lithospheric thickness we observe beneath Southern California. We chose to investigate two 2D models that capture the main characteristics of the crustal and lithospheric structure that we observe beneath the Salton Trough (evocative of sections D-D' and F-F' in Fig. 3). The synthetic dataset was designed to be smaller and sparser, but otherwise similar to the real dataset used in the study. We assumed a station spacing for this synthetic test of 33.5 km, which is similar to, but larger than that across the Salton Trough. We simulated waveforms for a set of ray parameters that is representative of our dataset (spanning 55° - 75° epicentral distances in 1° increments). Sources were assumed

to be coming from both the left and right sides of each model. This choice is similar to the roughly comparable number of Sp paths from the NW and SE in the real dataset relative to profile F-F', but over-emphasizes paths from the NE relative to profile D-D' because the real dataset is dominated by paths from the SW. However, the most significant difference between the synthetic tests and the backazimuth coverage afforded by the real dataset is that the latter contains a 3D distribution of sources.

The wave propagation simulations were started with a displacement S plane wave described by an error function with a rise time of 2 sec, chosen so that the deconvolved receiver functions have a similar, broad-band frequency content as those obtained from data. The synthetic velocity waveforms were then processed in the same way as the data and an image was obtained via the same CCP procedure explained in the Materials and Methods section, except that due to the much smaller number of waveforms considered, we no longer required >35 individual Sp receiver functions and determine a CCP stack at all points.

LAB and Moho discontinuities picked from the CCP stacks are shown in Figure S6. The top panel contains discontinuities roughly comparable to those in profile F-F'. Here LAB and Moho depths in the input model are accurately retrieved in the synthetic CCP stack, with discrepancies of less than 8 km (except for two points) which are within the uncertainties of the observed discontinuities. The bottom panel contains discontinuities comparable to those in profile D-D'. For this case, LAB and Moho depths are well-retrieved over much of the model, but the transitions in lithospheric thickness (which have a ~45° dip in the input model) appear over-steepened. This effect is due in part to secondary arrivals caused by wavefield interactions with the two zones of sloping LAB topography. However, even in the portion of the synthetic CCP stack where the input model is most poorly retrieved, the extent of thick lithosphere is over-estimated by no more than 40 km. Because the real dataset is dominated by sources from the NW and SE, it is reasonable to infer that actual resolution is more comparable to that in the first case (lower panel). Nonetheless, given the results of the second case (upper panel) interfaces which appear nearly vertical in the CCP stacks may in fact occur over roughly 40 km.

In both synthetic tests, the overall shapes of LAB and Moho topography are not systematically offset to the left or right from their locations in the input models. This result gives us confidence that the data and CCP stacking approach used in this study would be capable of discerning the lateral displacement of lithospheric thinning, crustal thinning, and surface extension that would occur if deformation was dominated by simple shear along shallow-dipping zones that are oriented in one direction and extend through both crust and mantle lithosphere (an asymmetric mode of deformation).

Automatic vs. hand picking of LAB phase

The map of LAB depth that we analyze is derived from the CCP Sp stacks via an automatic algorithm which identifies the LAB as the median depth of the 25 most negative values in the vertical CCP profile beneath each surface location in the 30 to 110 km depth range. The algorithm rejects CCP profiles and picks no LAB depth if any of the following are true: 1) more than 30% of the CCP vertical profile is sampled by fewer than 35 receiver functions; 2) more than 5 km of the CCP vertical profile in the 30-110 km depth range is sampled by fewer than 35 receiver functions; 3) the most negative phase is weaker than -0.04.

In order to ensure that the automatic LAB picking algorithm does not bias the interpretations of the CCP profiles, we compared its depth determinations against depths from user-defined LAB picks for each profile (selected as the peak of the largest and most robust negative phase below the Moho), and the center depth of a Gaussian fit to the CCP profile in the vicinity of the user-defined pick. Figure S7 shows scatterplots comparing LAB depths determined using these three procedures, demonstrating that automatic and hand-picking of LAB from the CCP stacks yield nearly identical results.

Comparing crustal and mantle stretching beneath the Salton Trough via an instantaneous stretching model

Assuming that pre-rift lithosphere remains beneath the study region, the thicknesses of the lithosphere and crust within the rift can be interpreted in terms of rifting-related stretching. However, crust and mantle lithosphere stretching estimates depend on assumptions about unrifted crust and lithosphere thicknesses, additions to the crust from sedimentation and magmatism, and removal of crust and mantle material through mechanical and thermal processes. We compared crustal and sediment thicknesses (27) to LAB depths across the ST and its margins. Unrifted crustal and lithospheric thicknesses were estimated to be 35 km and 80 km, respectively, based on typical values observed in the CCP stacks outside but adjacent to the Salton Trough. If sediment accumulation due to rift subsidence is taken to be the depth to basement, and no material has been added to the crustal basement, then crustal stretching in the ST ($\beta < \sim 2$) is systematically smaller than lithospheric stretching ($\delta = 2-3$) (Figure S8). However, if metamorphism of sediment and/or magmatism have increased apparent basement thickness (for example, if sediment addition is ~75-100% greater than apparent basement depths), lithospheric and crustal stretching estimates become comparable (δ between 2-3 and β predominantly between 1.5-3) (Figure S8).

Additions to crustal basement appear likely, although consensus does not exist on their origins. Interpretations of crustal velocity models have suggested that both metamorphism of sediment and mafic magmatism have made very substantial contributions to the volume of the crust (22,23). Recent estimates of sediment volume eroded in the Colorado River catchment since 5.3 Ma support the presence of significant metamorphosed sediment below the 5-6 km of unmetamorphosed sediment within the basin (49). On the other hand, geochemical data indicates that the layer of Salton Trough crust in between unmetamorphosed sediment and deep gabbroic basement was formed by rift-related basaltic melt intrusion with alteration by hydrothermal processes and additional partial melting (25).

Although we recognize the strong likelihood of mafic addition, and that crust and mantle stretching may differ, we explored whether crustal addition to the basement through sedimentation and metamorphism could by itself be consistent with uniform stretching of crustal basement and mantle. In particular, we tested whether the amount of subsidence expected for a given amount of crustal stretching is consistent with the amount of sediment necessary to render crustal and mantle lithosphere stretching estimates equal. The instantaneous stretching (pure shear) model (6) was used to predict the expected subsidence (S_i) for a given crustal stretching factor (β), assuming that areas below sea level get filled in by water or sediment of density ρ_w :

$$S_i = \frac{a \left[(\rho_0 - \rho_c) \frac{t_c}{a} \left(1 - \alpha T_1 \frac{t_c}{a} \right) - \frac{\alpha T_1 \rho_0}{2} \right] \left(1 - \frac{1}{\beta} \right)}{\rho_0 (1 - \alpha T_1) - \rho_w} \quad (1)$$

where ρ_0 is mantle density, ρ_c is crustal density, t_c is initial crustal thickness (taken to be 35 km), a is initial lithospheric thickness, α is the thermal expansion coefficient (taken to be $3.28 \times 10^{-5} \text{ }^\circ\text{C}^{-1}$), and T_1 is the temperature of asthenosphere (taken to be 1333°C). Because rifting in the Salton Trough is young, effects of diffusion of heat can be neglected (e.g. Fig 4 in 6).

For a range of crustal densities (2.6-3.1 g/cc), initial lithospheric thicknesses (60 – 140 km), and fill densities (1.5 – 2.6 g/cc), we calculated the expected sediment thickness for the crustal stretching factors determined from sections DD', EE', FF' and GG' (covering the Salton Trough and surrounding areas). We then calculated the sum of the squared differences between the predicted and observed/inferred sediment thicknesses and display them in Figure S9, where cool (warm) colors indicate good (poor) agreement. Two sets of crustal stretching factors and sediment thicknesses were explored: those determined for the depth to the basement from SCEC-CVM-H (27) (top panel of Figure S9), and those values from depth to basement plus 75%, (bottom panel of Figure S9). The latter case is required to bring crustal stretching factors in line with lithospheric stretching calculated from observed LAB depths, assuming that the initial LAB (before stretching) was at 80 km. Based on the results of this exercise (Figure S9), we conclude that both sediment scenarios (and their implied crustal stretching values) are equally plausible in the sense that sediment thicknesses calculated from the instantaneous stretching model provide equally good fits to observed/inferred sediment thicknesses. However, the enhanced sediment scenario requires greater fill densities, as would be expected if a large fraction of the sediment has been metamorphosed.

Measuring potential opening of the Salton Trough

We constrained possible opening of the Salton Trough based on the extent of thin lithosphere observed in the CCP stacks. Although the poor station coverage in northern Mexico limits where we robustly determine LAB depths to the southeast, estimates of opening are possible on a few profiles. In Figure S10, we plot a cross section oriented N60°W perpendicular to the strike of the boundary fault within the Salton Sea pull-apart basin (20). If the extent of new lithosphere is taken to be the area where lithospheric thicknesses are 50 km or less, there has been roughly 150 km of opening parallel to N60°W. This value is smaller than the ~300 km inferred for the northern Gulf of California (50). However, if the azimuth of opening varied over time, opening estimates from the CCP stacks would differ, and for certain azimuths only lower bounds would be obtainable.

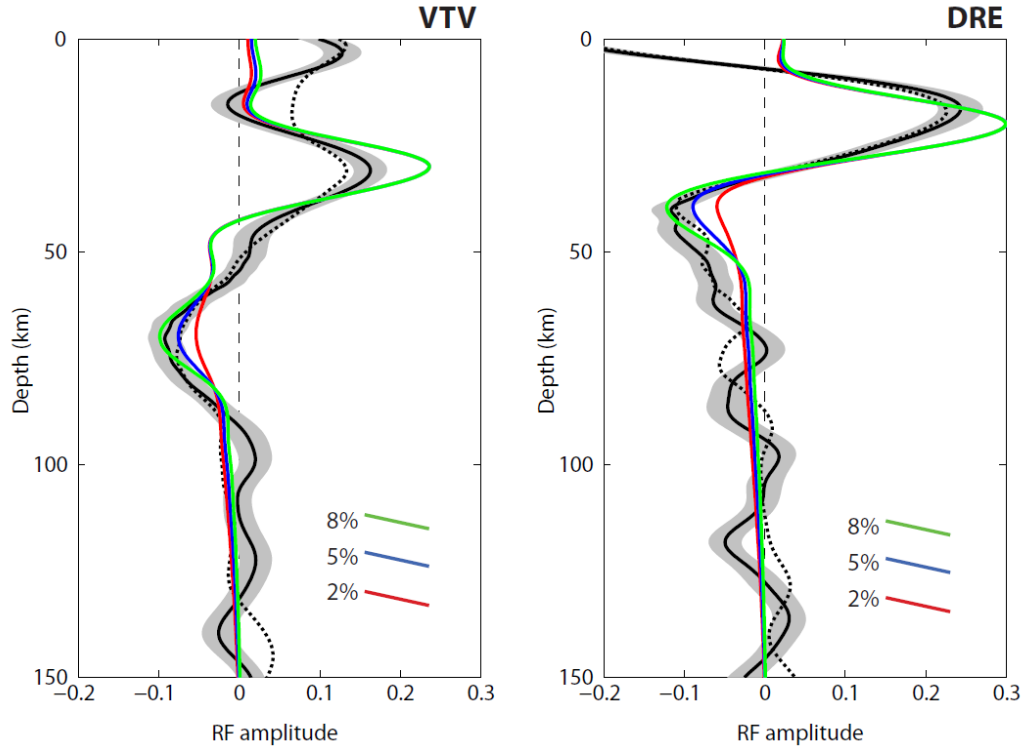


Fig. S1

Comparison of synthetic S_p receiver functions with those observed at VTV (Mojave) and DRE (Salton Trough). The solid black lines indicate the mean of the bootstrapped S_p receiver function, while shaded regions denote the 1σ error bounds from the bootstrapping. The colored lines correspond to S_p receiver functions constructed in an identical procedure, except from synthetic seismograms in one of two models: for VTV, Moho is at 30 km, LAB is at 70 km; for DRE, Moho is at 20 km and the LAB is at 40 km. In both cases, the velocity drop across the LAB is 2%, 5%, and 8%. The dashed solid black lines are the CCP stack values directly beneath each station. The strength of the LAB phases on the station stacks require a velocity drop of more than 5%, and they are best fit by 8%, which accounts for most of the total velocity drop from the lithosphere into the asthenosphere determined from regional tomographic models. We note that while the LAB phase in the VTV CCP stack is somewhat weaker and deeper than in the single-station stack (although still within the station stack 1σ error bars), its amplitude is nevertheless sufficiently large to associate it with the lithosphere-asthenosphere boundary.

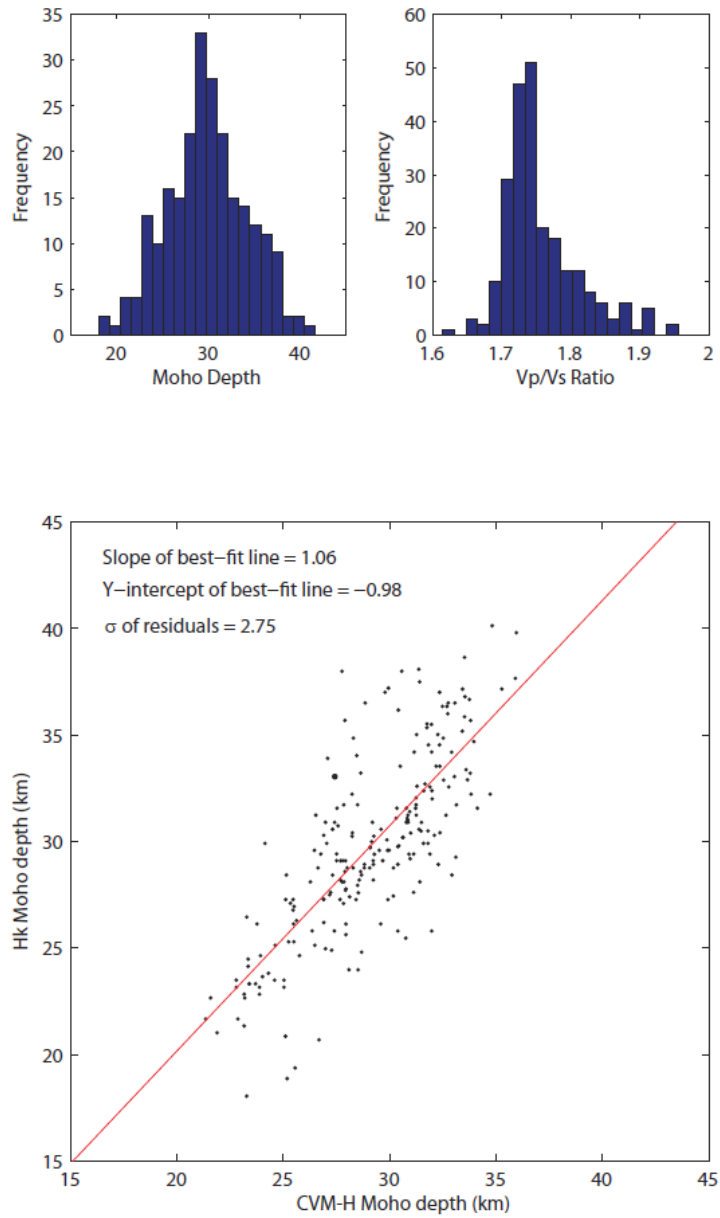


Fig. S2

(top) Histograms of Moho depths (left) and Vp/Vs ratios (right) determined by H- κ stacking of teleseismic Ps receiver functions beneath the stations used in this study. (bottom) Comparison of crustal thicknesses from our study with those from the SCEC-CVM-H model (27). The best fit line is plotted in red.

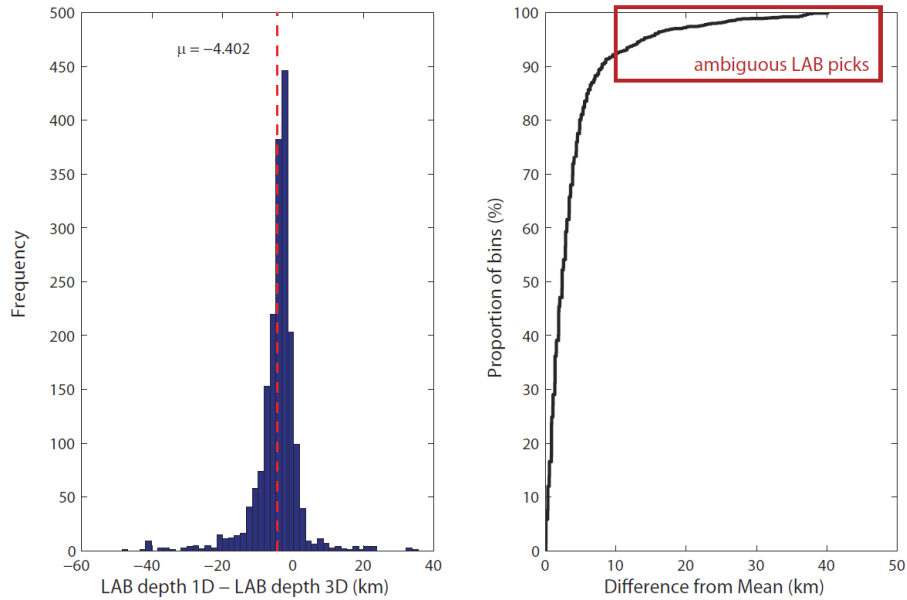


Fig. S3

The maximum likely difference in LAB depth arising from migration through inaccurate crustal and mantle velocity structure. LAB depths determined from migration through the 1D SCEC model (46) for the crust and AK135 (47) for the mantle are subtracted from LAB depths determined from migration through our preferred 3D model. (left) Histogram of differences in LAB depth which is strongly peaked around the mean bias of 4.4 km. (right) Plot showing the proportion of all bins in which the difference in LAB depth is within the specified distance from this mean. The <5% of locations in which changing the migration model leads to very different LAB depths are associated with regions where the identification of an LAB phase is ambiguous and should not be interpreted to represent true uncertainty on LAB depth due to velocity structure.

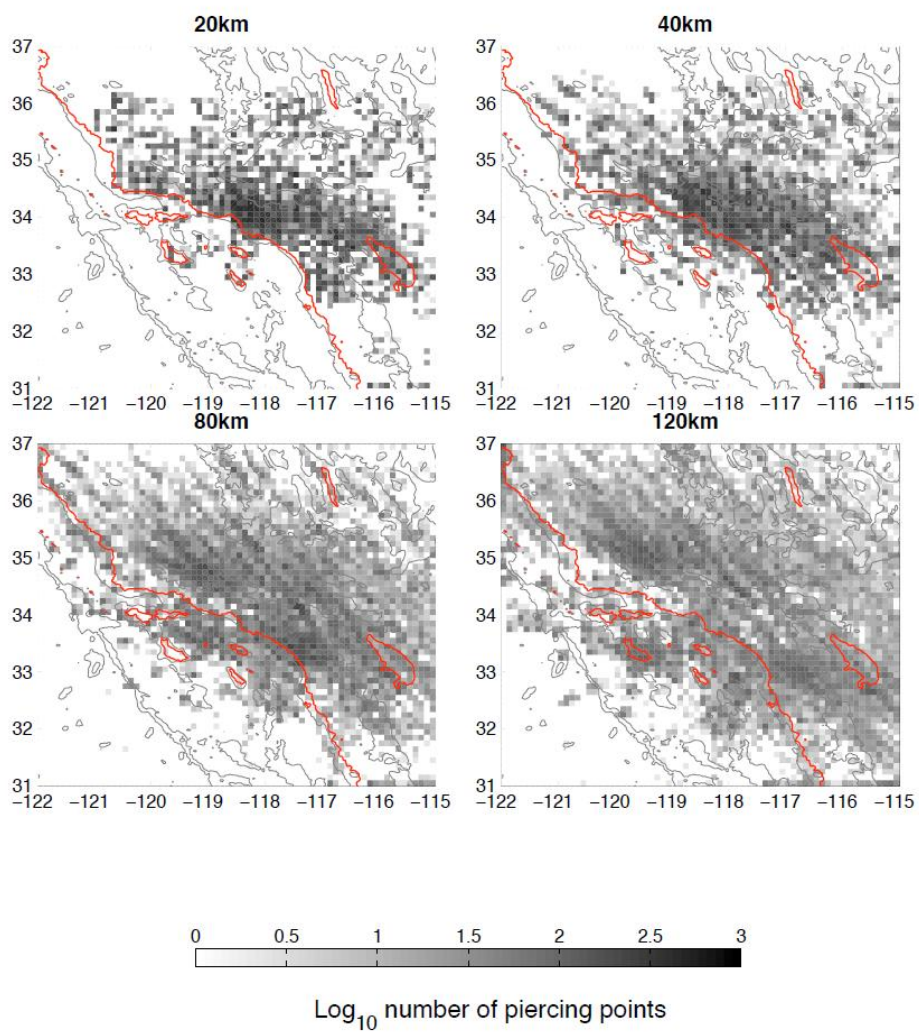


Fig. S4.
 Number of Sp ray paths that fall within each block of the CCP stack at four different depths.

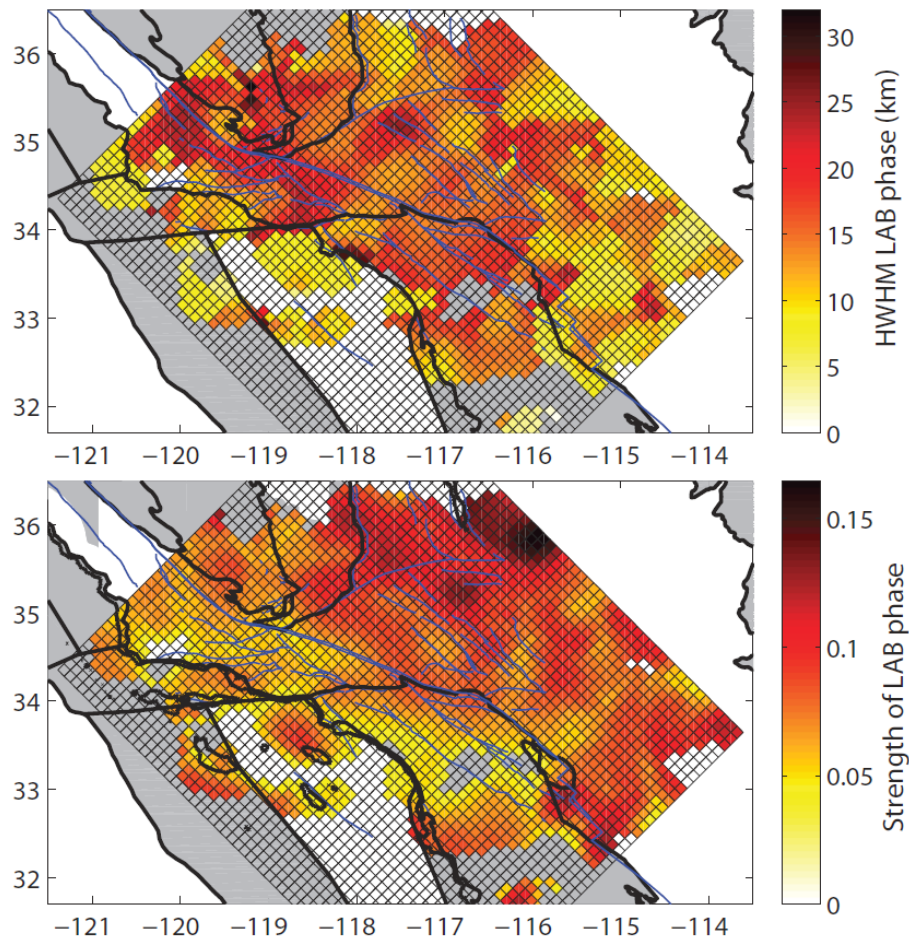


Fig. S5

(top) Half-width half-maximum of the LAB phase beneath each point of our model. Half of this value represents a reasonable upper limit on uncertainty in LAB depth determination due to the band-limited frequency content of the Sp receiver functions.
 (bottom) Map of the strength of the LAB phase.

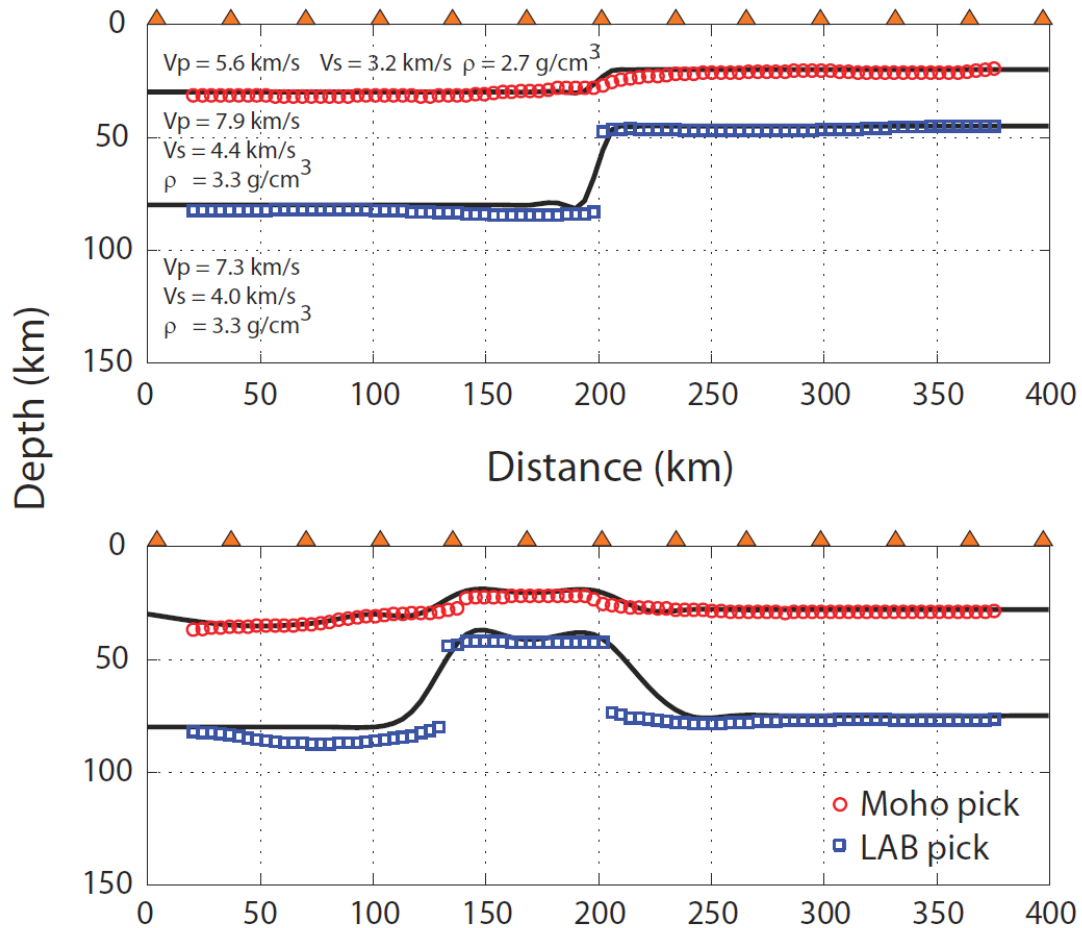


Fig. S6

LAB (blue squares) and Moho (red circles) discontinuities picked from the CCP stacks obtained from synthetic waveforms calculated at 13 stations (orange triangles) using SPEC-FEM2D. The input velocity structure consists of three regions, denoted by black lines: crust, mantle lithosphere, and asthenosphere. LAB and Moho depths are accurately retrieved for both types of structures, with the exception that the increases in lithospheric thickness appear over-steepened, particularly in the bottom panel (analogous to profile DD'). In the top panel (analogous to profile FF' and roughly parallel to the direction of extension), retrieved LAB topography is not shifted with respect to surface features, confirming our ability to discriminate between symmetric and anti-symmetric modes of deformation.

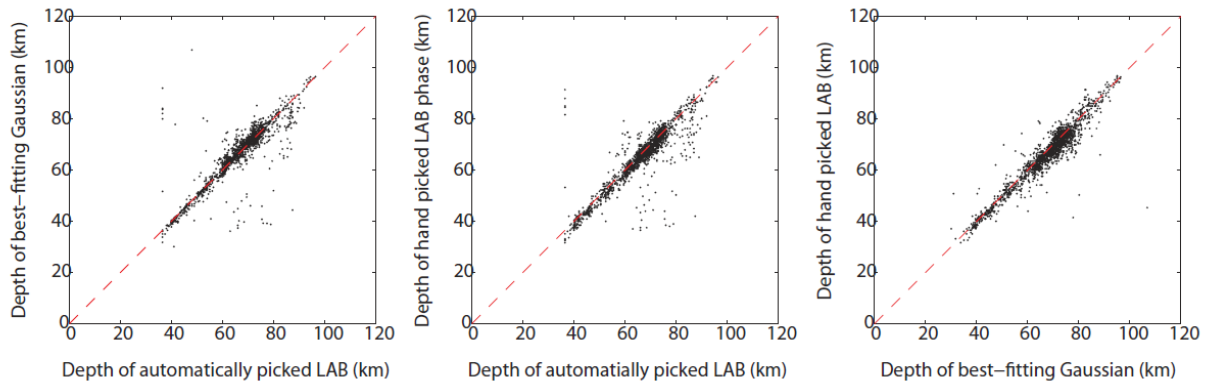


Fig. S7

Comparisons between LAB depths determined by three methods: (left to right) automatic picking algorithm described in the text, user-selected depth of maximum robust negative phase below the Moho, depth of the center of the best-fit Gaussian in the vicinity of the user LAB depth pick.

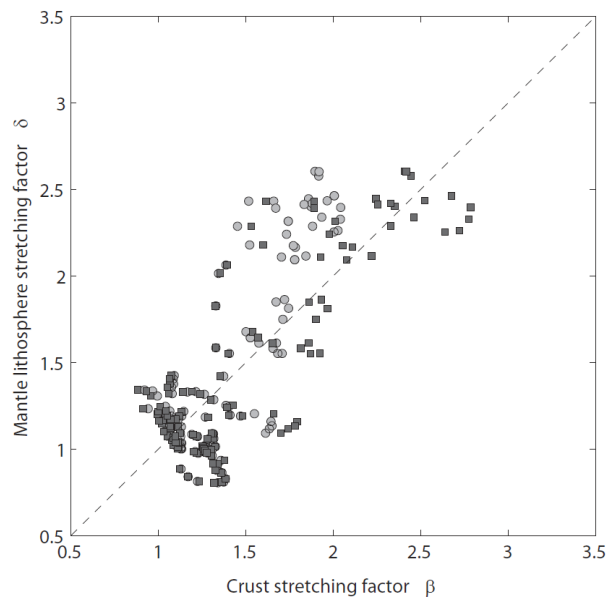


Fig. S8

Lithospheric stretching factors for the Salton Trough. (a) Observed crustal thinning factors assuming that accumulated sediment in the Salton Trough is represented by depth to basement (27) (circles) or depth to apparent basement plus 75% (squares). Unextended crustal and mantle lithosphere thicknesses are taken to be 35 and 45 km, respectively. Values correspond to individual model bins from sections in Fig. 3. Values of ~1-1.5 are from outside the ST.

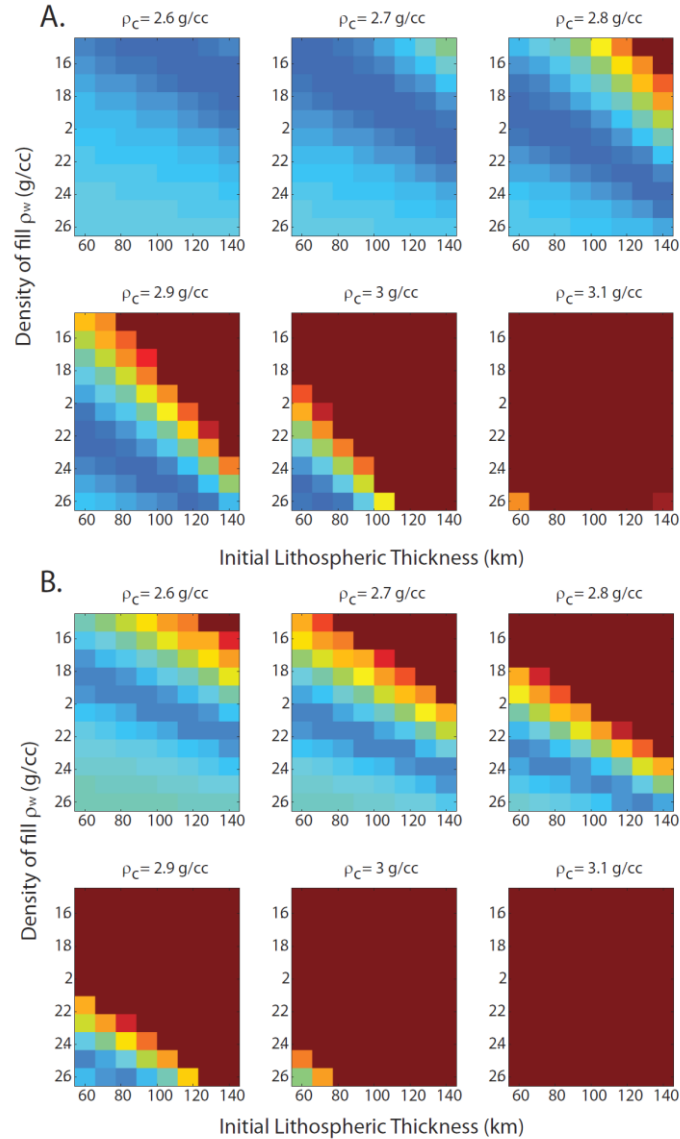


Fig. S9

Misfit between observed/inferred and predicted sediment thicknesses for two scenarios: A. sediment thickness is equal to the depth to basement; B. sediment thickness is 75% greater than in A. Sediment thicknesses are predicted from crustal stretching factors corresponding to the two scenarios using the instantaneous stretching model (6). Cool (warm) colors denote good (poor) fit.

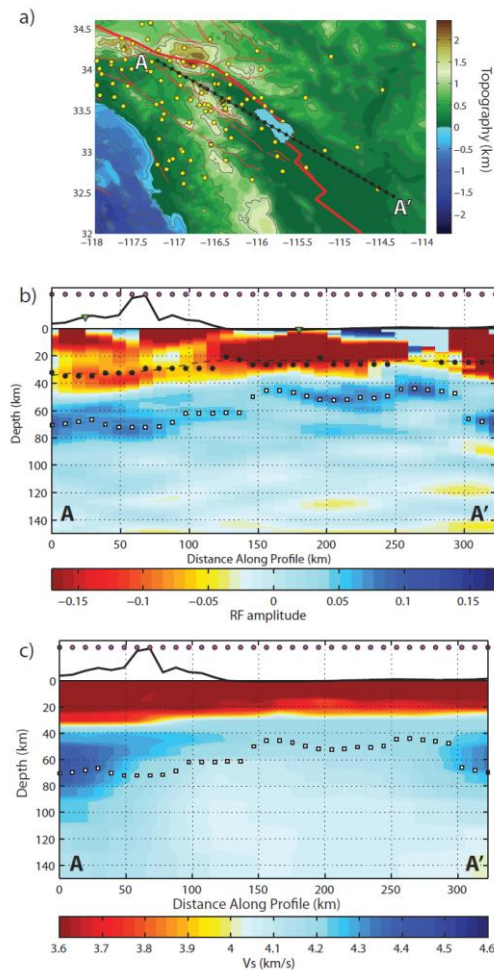


Fig. S10

Type (a) Map of the Salton Trough shows main faults (red lines), seismic stations (yellow dots), and the surface trace of vertical cross-section through the CCP model (black, dotted line) trending N60°W, parallel to direction of recent extension (20). (b) Vertical section through the CCP stack indicates that the zone of thinned lithosphere (LAB depth 40-50 km) extends ~150 km (symbols are same as in Figure 2). Warm colors indicate a velocity increase with depth; at depths of less than 40 km these interfaces correspond to the base of sediment or crust. Cool colors indicate a velocity decrease with depth; we interpret the largest amplitude velocity decrease as the LAB. Green triangles indicate surface traces of faults. Surface topography (black line) is exaggerated 10-fold. Dashed black lines trace the Moho (27), while black dots indicate closest Moho depths from H-k stacking. White squares denote auto-picked LAB depth. Note that in this and other sections, Moho depth does not always align with the maximum amplitude of the warm colors due to interference between sediment and Moho Sp phases. (c) Vertical section through an absolute Vs model from Rayleigh wave tomography (10) in which low mantle velocities correlate with thin lithosphere and high mantle velocities with thick lithosphere.